catalysts

MDPI

Article

Preparation of Bi_2WO_6/MXene($Ti_3C_2T_x$) Composite Material and Its Photothermal Catalytic Reduction of CO_2 in Air

Lingji Zhang [1], Mengke Shi [1], Shuo Zhang [1], Feng Yue [1], Cairong Yang [1], Yang Meng [1,2], Wen Li [1], Cong Li [1,2], Mario Berrettoni [2], Silvia Zamponi [2], Yongpeng Ma [1,*] and Hongzhong Zhang [1,*]

[1] Henan Collaborative Innovation Center of Environmental Pollution Control and Ecological Restoration, Zhengzhou University of Light Industry, Zhengzhou 450001, China; lingjizhang136@163.com (L.Z.); mengkeshi2000@163.com (M.S.); zshuo1999@163.com (S.Z.); yuefeng199808@163.com (F.Y.); cairongyang0126@163.com (C.Y.); yangmeng19951122@163.com (Y.M.); wenli_echo@163.com (W.L.); cong.li@unicam.it (C.L.)

[2] Department of Chemistry, University of Camerino, Camerino, 62032 Macerata, Italy; mario.berrettoni@unicam.it (M.B.); silvia.zamponi@unicam.it (S.Z.)

* Correspondence: mayongpeng1984@163.com (Y.M.); zhz@zzuli.edu.cn (H.Z.)

Abstract: In response to growing concerns about the greenhouse effect, the direct conversion of atmospheric CO_2 has become a pivotal research focus. This research utilizes hydrothermal synthesis to develop Bi_2WO_6/MXene($Ti_3C_2T_x$), which efficiently reduces CO_2 directly at the gas–solid interface through photothermal synergy, without requiring additional sacrificial agents or alkaline absorption solutions. The results indicate that the CO formation rate is about 216.9 $\mu mol \cdot g^{-1}h^{-1}$. Notably, this system demonstrates exceptional selectivity for reducing CO_2 to CO. The outstanding photothermal catalytic efficiency is attributed to the introduction of MXene, which serves as an efficient and economical co-catalyst. The integration of MXene improves the composite material's specific surface area and pore structure, enhances its CO_2 adsorption capacity, and results in the Bi_2WO_6/MXene hybrid having a shorter charge transfer distance and a larger interface contact area. This ensures superior charge transfer capabilities, ultimately leading to a significant enhancement in the catalytic efficiency of the composite. This study presents a straightforward and highly selective method for capturing and converting atmospheric CO_2, offering fresh insights for developing efficient photothermal catalytic materials.

Keywords: Bi_2WO_6/MXene; photothermal catalytic; CO_2 reduction; gas–solid interface; atmospheric CO_2 capture

Citation: Zhang, L.; Shi, M.; Zhang, S.; Yue, F.; Yang, C.; Meng, Y.; Li, W.; Li, C.; Berrettoni, M.; Zamponi, S.; et al. Preparation of Bi_2WO_6/MXene($Ti_3C_2T_x$) Composite Material and Its Photothermal Catalytic Reduction of CO_2 in Air. *Catalysts* **2024**, *14*, 859. https://doi.org/10.3390/catal14120859

Academic Editor: Benoît Louis

Received: 31 October 2024
Revised: 22 November 2024
Accepted: 23 November 2024
Published: 26 November 2024

1. Introduction

As the global population grows rapidly and industrialization advances across countries, carbon dioxide (CO_2) emissions have been rising annually [1]. Over the past three decades, the extensive use of fossil fuels has led to significant environmental impacts, environmental pollution has worsened, and resources are becoming increasingly scarce. The massive release of carbon dioxide not only intensifies global warming but also leads to environmental issues like climate change and ecosystem imbalance [2,3]. In response to these challenges, many nations are exploring effective emission reduction strategies [4–6]. The photocatalytic conversion and utilization of CO_2, recognized as a clean and sustainable approach, holds great promise for mitigating the greenhouse effect [7–9]. Studies indicate that the current atmospheric CO_2 concentration has reached an average of 420 ppm. Capturing atmospheric CO_2 and converting it into valuable hydrocarbon fuels could serve as an abundant, renewable carbon source, offering new opportunities for carbon recycling and reducing greenhouse gas emissions [10].

In this global context, scholars from various countries have invested in the research of CO_2 emission reduction technology [11]. The CO_2 reduction reaction can be divided

into three categories according to its energy source: thermal catalysis, photocatalysis, and electrocatalysis [12,13]. A single catalytic condition has certain limitations, such as high energy consumption and difficulty in regulating product selectivity [14]. To address these challenges, recent research has increasingly focused on photothermal catalysis technology. This approach combines the advantages of photocatalysis and thermocatalysis, coupling light and heat energy to effectively modulate the activity and selectivity of CO_2 reduction [15,16]. Photothermal catalytic CO_2 reduction technology has emerged as a research hotspot in the field of energy and environmental protection, owing to its high efficiency and environmentally friendly characteristics [17]. It holds significant potential for practical applications and offers innovative solutions for addressing the worldwide energy crisis and environmental issues [18–20].

In recent years, bismuth tungstate (Bi_2WO_6) with a perovskite structure has attracted substantial interest due to its remarkable photochemical stability, eco-friendliness, and cost-effectiveness. These qualities position it as a strong candidate for diverse catalytic and environmental application [21,22]. For example, Cao et al.'s [23] Ti_3C_2/Bi_2WO_6 nanosheets were successfully synthesized through in-situ growth using a hydrothermal method and successfully converted into CH_4 and CH_3OH, demonstrating exceptional photocatalytic performance. Ju et al. [24] fabricated a $Bi_2WO_6/BiVO_4$ heterojunction through calcination, enhancing photocatalytic reduction efficiency and achieving 100% degradation of rhodamine B within 30 min. Liu et al.'s [25] series of $P25/Bi_2WO_6$ nanocomposites were synthesized by a one-step hydrothermal method. The generation of heterojunction enhances the utilization of sunlight and promotes the photoreduction of CO_2 to CO. However, Bi_2WO_6 materials still face certain challenges in practical applications, including the rapid recombination of photo-induced electron-hole pairs and a relatively low affinity for CO_2 molecules, which limit their catalytic performance [26]. To address these limitations, researchers have aimed to enhance the mobility of photo-induced charge carriers and augment the active sites on the catalyst surface by incorporating noble metals like Pt, Au, and Ag [27]. However, due to the scarcity and high cost of noble metals, their application is limited, making the exploration of non-noble metal co-catalysts a significant research focus in the field of CO_2 reduction. Since its introduction in 2011, MXene($Ti_3C_2T_x$) has garnered widespread attention in the field of catalysis, particularly for its impressive photothermal conversion capabilities and unique material properties [28,29]. Studies indicate that MXene features surfaces densely populated with active sites, which promote efficient light absorption and effective thermal conductivity [30–32]. Based on these characteristics, this study combines bismuth tungstate (Bi_2WO_6) with MXene to design a novel photothermal catalyst. The catalyst leverages strong structural and electronic coupling effects at the interface, enhancing the efficiency of electron-hole separation. This facilitates the selective conversion of CO_2 into valuable chemicals, such as carbon monoxide (CO). The catalyst achieves a CO generation rate of 216.9 $\mu mol \cdot g^{-1} \cdot h^{-1}$, demonstrating excellent photothermal catalytic performance. The reaction system under study operates at the gas–solid interface, distinct from conventional solid–liquid catalytic systems. This innovative approach eliminates the need for organic solvents and sacrificial agents, offering a sustainable and cost-effective solution for CO_2 reduction. Moreover, the system directly utilizes atmospheric CO_2, reducing it to carbon monoxide with high selectivity. This process effectively reduces greenhouse gas emissions and generates CO, which serves as a vital raw material for chemical manufacturing, metallurgy, and other industries, thereby lowering production costs and further promoting the development of green chemistry.

2. Results and Discussion

2.1. Phase Structure of Catalysts

In this study, we conducted a qualitative analysis of the crystal phases of MXene and its composites at various molar ratios using X-ray diffraction (XRD) spectroscopy. As shown in Figure 1A, distinct peaks are observed at $2\theta = 18.3^\circ$ and 60.8°, which are indicative of the HF etching of MXene. These peaks correspond to the (004) and (110) crystal

planes of MXene, confirming the successful etching and preparation of the material [33]. Additionally, the figure clearly shows four prominent diffraction peaks for BW at 2θ = 28.3°, 32.79°, 47.158°, and 55.832°, corresponding to the (113), (200), (220), and (313) crystal planes, respectively, with JCPDS card number 73-1126. These results confirm the successful synthesis of surface BW.

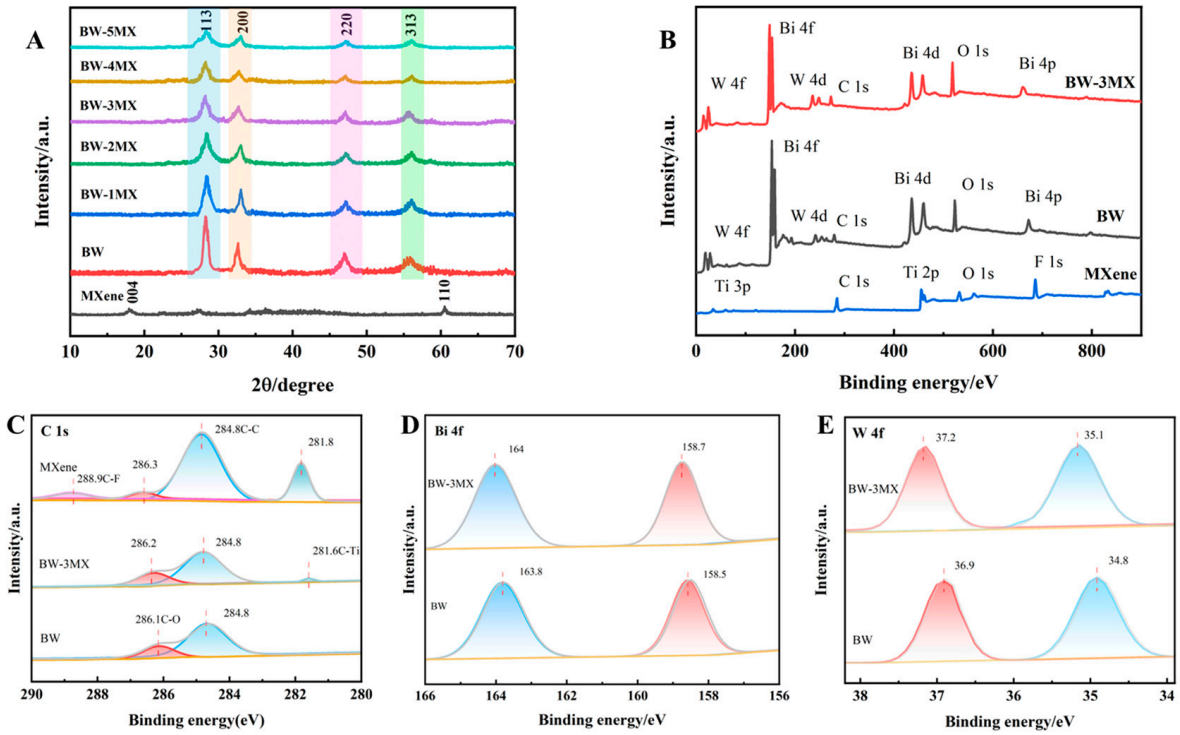

Figure 1. XRD patterns (**A**) of BW/MX and MXene; XPS spectra ((**B**) Survey) of MXene, BW and BW-3MX; XPS spectra ((**C**) C 1s; (**D**) Bi 4f; (**E**) W 4f) of BW-3MX.

By comparing the XRD patterns of composites with different ratios, we observed that as the MXene content in the BW matrix increases, the intensity of all relevant diffraction peaks in the BW-MX composite XRD spectra decreases [34]. This phenomenon is attributed to the growth inhibition of MXene, which consequently restricts the further development of BW microcrystals [35]. The absence of a distinct MXene diffraction peak in the spectrum is likely due to the relatively low content of MXene and its uniform distribution within the composite, rendering its characteristic signal undetectable in the XRD analysis.

To further examine the surface state and chemical composition of the composite material, X-ray photoelectron spectroscopy (XPS) characterization was conducted [33]. Figure 1B presents the XPS spectra of MXene, Bi_2WO_6, and the BW-3MX composite. The XPS analysis of MXene reveals that it primarily consists of Ti, C, O, and F elements, confirming the complete etching of Al [36]. In the XPS spectrum of BW-3MX, we detected all elements associated with both MXene and Bi_2WO_6 (Bi, W, Ti, C, and O). Furthermore, Figure 1C shows the C 1s spectrogram of MXene, BW, and BW-3MX. All binding energies were calibrated using the C 1s peak at 284.8 eV, attributed to adventitious carbon (C-C). In BW, the peak at 286.1 eV represents the C-O bond [37]. For the BW-3MX composite, characteristic peaks at 281.6 eV and 286.2 eV indicate C-Ti and C-O bonds [38]. The MXene spectrum features peaks at 281.8 eV, 286.3 eV, and 288.9 eV, representing C-Ti, C-O, and C-F bonds [39]. A 0.2 eV negative shift in C-Ti and C-O binding energies in BW-3MX compared to MXene suggests enhanced interactions between MXene and Bi_2WO_6 within the composite [40]. Conversely, the Bi 4f spectra of BW and BW-3MX (Figure 1D) show an opposite trend. In BW, the Bi 4f binding energies are observed at 163.8 eV and 158.5 eV, while in BW-3MX, the peaks shift to 164.0 eV and 158.7 eV, respectively. Additionally, the

W 4f spectra (Figure 1E) exhibit a similar positive shift in BW-3MX compared to BW [41]. These results indicate that electron transfer occurs from Bi_2WO_6 to MXene, implying strong interfacial interactions between the ultrathin nanosheets of MXene and Bi_2WO_6. Furthermore, the absence of C-F and Ti-F bonds in BW-3MX indicates that terminal F atoms have been substituted with -O or -OH groups. This modification improves the capability of MXene to capture photogenerated electrons from Bi_2WO_6, thereby improving the photocatalytic efficiency of the composite.

2.2. Morphology Structure Characterization of Catalysts

Scanning electron microscopy (SEM) was employed to examine the microstructure of the catalyst, as illustrated in Figure 2A,B. The MXene sample displays a distinctive accordion-like morphology, characteristic of its layered structure, whereas Bi_2WO_6 forms as nanosheets with irregular thickness. The SEM image of the Bi_2WO_6/MXene nanosheet composite (Figure 2C) clearly shows that the two-dimensional Bi_2WO_6 nanosheets can be directly grown on the surface of MXene, indicating a strong interfacial interaction between the two materials.

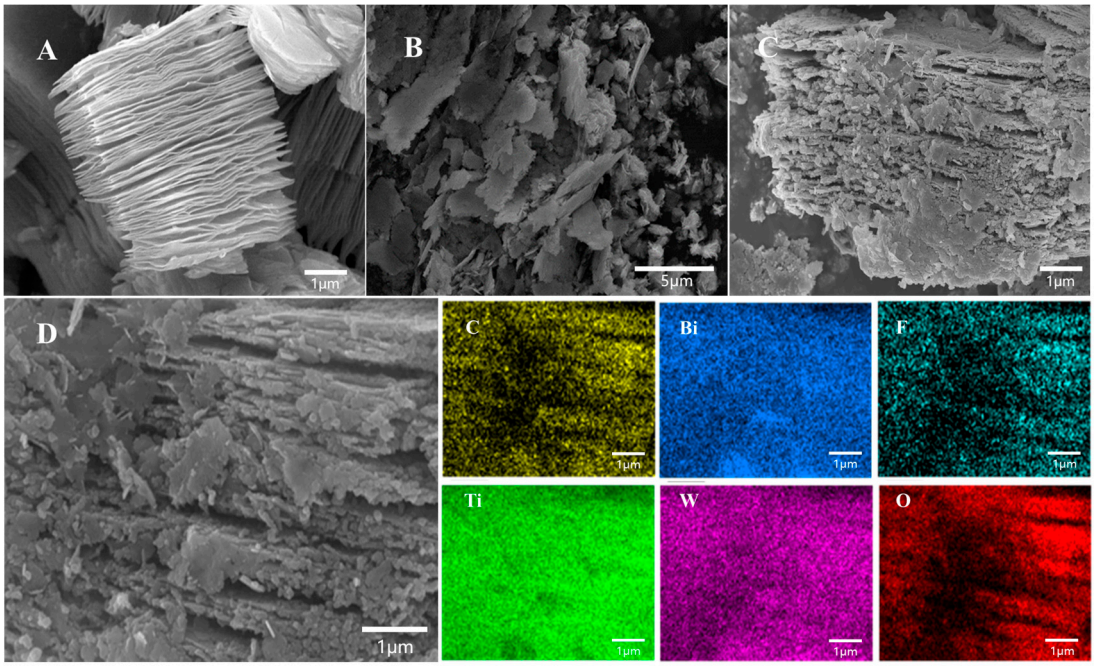

Figure 2. SEM images (**A**) MXene; (**B**) Bi_2WO_6; (**C**) BW-3MX) and EDS images (**D**) of Bi_2WO_6.

To analyze the elemental composition and spatial distribution within the catalyst, this study employed energy-dispersive X-ray spectroscopy (EDS), with the results presented in Figure 2D. The elemental mapping confirms that the composite (BW-3MX) consists of uniformly distributed Ti, O, F, C, Bi, and W. This result confirms the successful and uniform dispersion of Bi_2WO_6 across both the surface and interlayer regions of the MXene structure. Such homogeneous dispersion is crucial for promoting efficient interfacial interactions, thereby improving the photocatalytic performance of the composite material.

Transmission electron microscopy (TEM) was further employed to characterize the lattice spacing and internal structure of the BW-3MX composite. Figure 3A,B show low-resolution images revealing that Bi_2WO_6 crystals are layered onto the MXene sheets, attributed to ultrasonic pretreatment that exfoliates the layered MXene into thin sheets. The high-resolution image shown in Figure 3C clearly displays the lattice fringes of the nanocrystals in the Bi_2WO_6 and MXene samples. The interplanar distance of 0.315 nm corresponds to the (113) crystal plane of Bi_2WO_6, while the spacing of 0.253 nm matches the (002) plane of MXene. These distinct lattice fringes verify the effective nanoscale integration

of Bi_2WO_6 and MXene, which plays a vital role in enhancing the composite's photo-thermal catalytic performances by enabling efficient interfacial charge transfer.

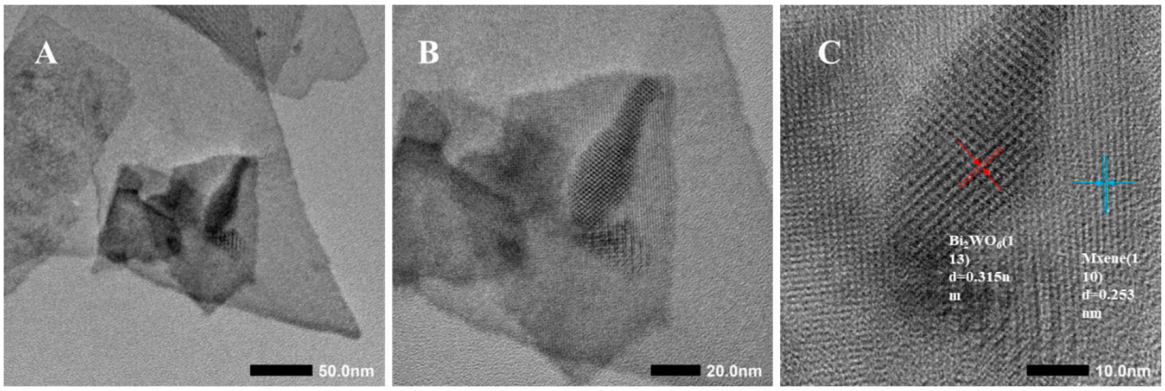

Figure 3. TEM images (**A**,**B**), HRTEM image (**C**) of BW-3MX.

2.3. Photoelectrochemical Characterization of Catalysts

To investigate the optical absorption properties of the synthesized samples, we employed UV-visible diffuse reflectance spectroscopy (DRS). As shown in Figure 4A, regardless of the amount of MXene added, the absorption edge of Bi_2WO_6 remains essentially unchanged. This suggests that no significant doping effect occurred during the hybridization process. Notably, the absorption intensity within the 420–600 nm range increases with greater MXene content, likely due to the broad-spectrum absorption of MXene, which enhances the material's overall light absorption capacity. The darkening of the sample color as more MXene is added also supports this observation, indicating that the incorporation of MXene significantly improves the material's ability to harness sunlight.

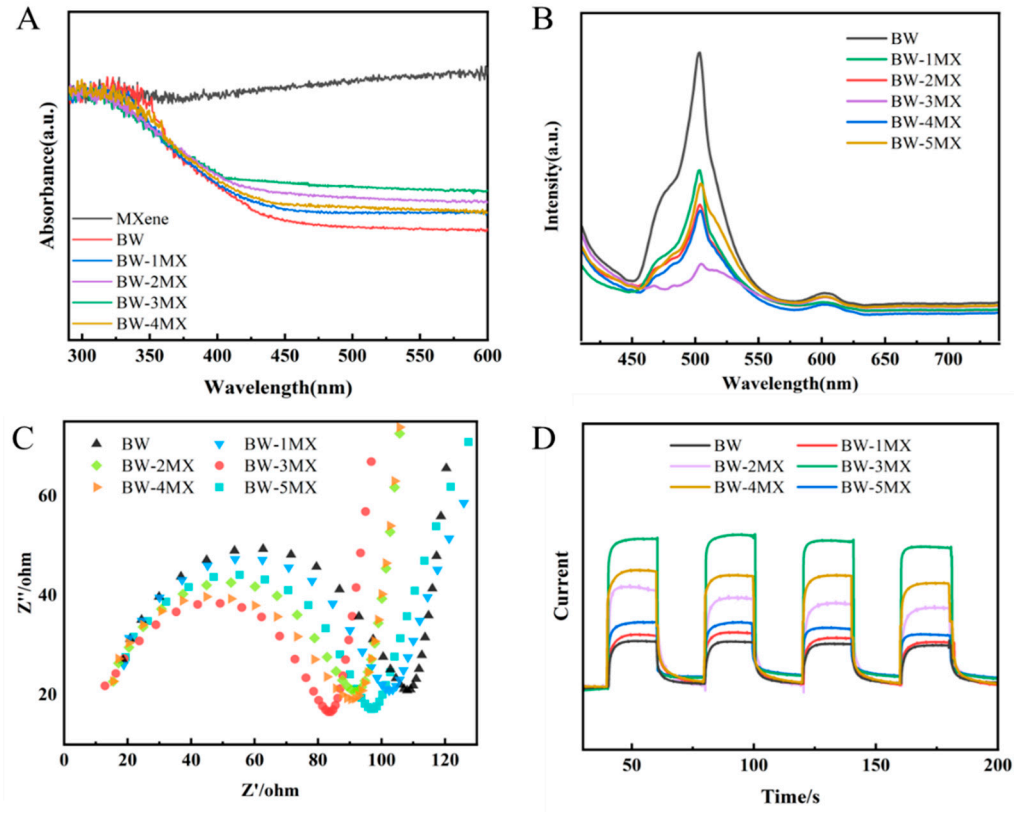

Figure 4. UV–Vis DRS (**A**), PL spectra (**B**), EIS spectra (**C**) of catalysts; photocurrent response spectra (**D**).

Based on the photoluminescence (PL) generation mechanism, PL can be classified into excitonic photoluminescence and band-edge photoluminescence [42]. The weak PL signal indicates a lower electron-hole recombination rate, meaning a longer carrier lifetime and, consequently, higher catalytic efficiency. The height of the emission peak diminishes with increasing MXene loading. Notably, BW-3MX shows the lowest fluorescence intensity, suggesting that an optimal amount of MXene can effectively reduce the recombination rate of photogenerated carriers, thereby enhancing catalytic efficiency [43].

To further elucidate the enhanced synergistic mechanism between MXene and Bi_2WO_6, electrochemical impedance spectroscopy (EIS) analysis was conducted. As shown in Figure 4C, doping with MXene results in a marked decrease in the arc radius, indicating that an optimal amount of MXene effectively enhances charge transfer dynamics [44]. Notably, BW-3MX demonstrates the smallest arc radius, indicative of the lowest charge transfer resistance among the samples tested. Consequently, the integration of MXene into the composite significantly enhances the mobility of photogenerated carriers, thereby facilitating a faster photocatalytic reaction rate.

Photocurrent is generated through electrons produced by electron-hole pairs under diffused illumination. Upon activation of the light source, there is a rapid increase in photocurrent density, and upon turning off the light source, it quickly returns to a low initial value. The transient photocurrent response of different proportions of loaded materials and the original Bi_2WO_6 was measured, with the results shown in Figure 4D. As expected, BW exhibits a lower photocurrent response. However, the addition of MXene significantly enhances the photocurrent response, with BW-3MX showing a substantially higher response than BW, indicating improved carrier separation in the hybrid material.

The optical energy gap (E-g) of the catalysts was determined using the Kubelka–Munk (K–M) function, a widely adopted method for analyzing diffuse reflectance data. As illustrated in Figure S1A–F, this approach enables accurate estimation of E-g values, providing insight into the electronic properties of the prepared catalysts. The E-g values for BW, BW-1MX, BW-2MX, BW-3MX, BW-4MX, and BW-5MX are 3.05 eV, 2.85 eV, 2.81 eV, 2.77 eV, 2.91 eV, and 2.95 eV, respectively. The results show that the E-g of the catalyst changes due to the loading of MXene. To further elucidate, the flat-band potentials of each catalyst were determined using Mott–Schottky (M–S) plots in Figure S2A–F, revealing the specific band structure. Notably, the positive slopes observed in the M–S curves across different frequencies (500–1500 Hz) confirm that bismuth tungstate exhibits characteristic behavior as an n-type semiconductor, revealing the specific band structure (Figure S3).

2.4. Absorption–Desorption and Pore Size Analysis

The pore size distribution and specific surface area of the synthesized samples were evaluated through N_2 adsorption–desorption isotherm analysis. As shown in Figure 5A, the results indicate that the N_2 adsorption capacity of BW-3MX is significantly higher than that of pure BW. This increase in adsorption capacity is attributed to the loading of MXene, which enhances the specific surface area of BW, providing more active sites for adsorption and surface reactions [45]. However, it was observed that excessive loading of MXene can result in a decrease in specific surface area, suggesting that an optimal loading amount is required. By comparing the pore sizes in Figure 5B, it is evident that the pore volume increases after MXene loading. Consequently, it provides a wealth of active surface sites to enhance adsorption processes. This increase in pore volume is beneficial for facilitating further reactions, indicating that MXene can serve as an effective co-catalyst. Figure 5C also shows the CO_2 adsorption capacity of the materials. The CO_2 adsorption curve of BW-3MX is noticeably superior to the other samples. In the low-pressure region, the BW-3MX curve rises much more rapidly than the others, likely due to the presence of micropores. As the relative pressure increases, differences in specific surface area and pore volume become more apparent between the samples. At $P/P_0 = 1.0$, the CO_2 adsorption capacities for BW, BW-1MX, BW-2MX, BW-3MX, BW-4MX, and BW-5MX are 0.98, 1.3, 2.17, 3.95, 1.89, and 1.55 cm^3g^{-1}, respectively.

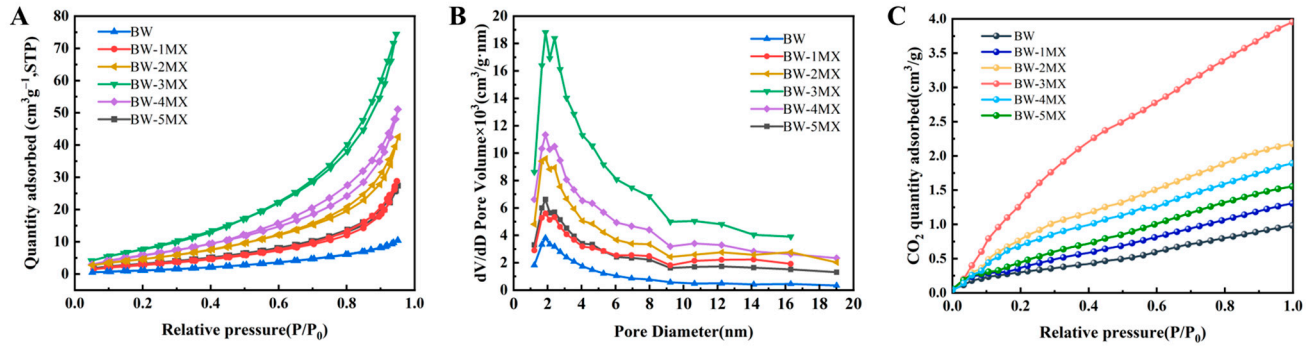

Figure 5. N_2 adsorption–desorption isotherms and pore size distributions (**A**,**B**); CO_2 adsorption curves (**C**).

These results suggest that the ultrathin BW-3MX, with a larger specific surface area and pore width, exhibits superior CO_2 affinity, which in turn enhances surface reaction kinetics. The calculation shows that the BW-3MX composite can absorb about 97 ppm CO_2 in the reactor (5 mg catalyst). Therefore, assuming the CO_2 originates from ambient air, the initial concentration of CO_2 in the reactor can be estimated to be 517 ppm.

2.5. Analysis and Stability Test of Photocatalytic Reduction of CO_2

For the BW sample, the CO_2 reduction efficiency was initially evaluated under solar illumination at 25 °C. Following a four-hour reaction period, BW-3MX demonstrated the highest photocatalytic activity, and its CO production was 312.8 μmol·g^{-1}, with a CO generation rate of 78 μmol·g^{-1}·h^{-1}, as shown in Figure 6A. This CO output surpassed that of BW by a factor of 2.7. Subsequently, to evaluate the light stability, six experimental cycles were performed, as shown in Figure 6D. At the conclusion of the sixth cycle, the CO yield accounted for over 70% of the initial yield, indicative of excellent photocatalytic stability.

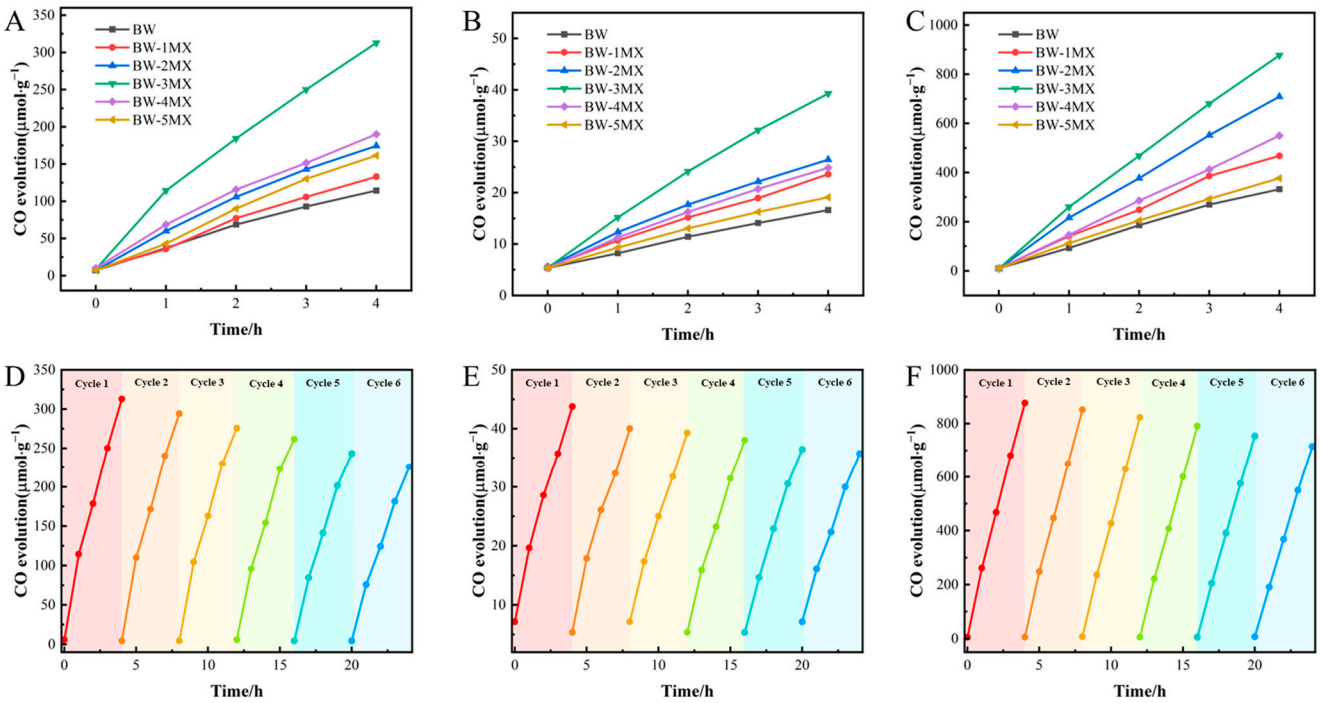

Figure 6. Performance diagram (**A**,**D**) photocatalytic performance and stability; (**B**,**E**) thermal catalytic performance and stability; (**C**,**F**) photothermal catalytic performance and stability).

2.6. Analysis and Stability Test of Thermal Catalysis Reduction of CO_2

Conducting a catalytic experiment at 80 °C under dark conditions, we delved into assessing the catalytic reduction capabilities of various composite material ratios. Figure 6B shows the performance of the BW-3MX catalyst. After 4 h of reaction, the production of CO is 46.5 $\mu mol \cdot g^{-1}$. Comparing it to the BW under identical experimental conditions, the BW-3MX's productivity soared to 2.6 times that of its counterpart. To further verify its stability, we conducted six cycles of the experiment, each lasting four hours. As shown in Figure 6E, the BW-3MX catalyst managed to produce 35.8 $\mu mol \cdot g^{-1}$ of CO, retaining 77% of its initial output. This performance underscores its thermal stability and reinforces its potential for practical applications.

2.7. CO_2 Photothermal Catalytic Reduction Analysis and Stability Test

In an innovative approach that fuses photocatalysis with thermocatalysis, a reaction setup has been devised to maintain a stable temperature of 80 °C within the reaction chamber, enhancing the harnessing of electrons and solar energy at the gas–solid interface. As depicted in Figure 6C, this hybrid system exhibits exceptional photothermal catalytic performance, yielding an impressive 876.7 $\mu mol \cdot g^{-1}$ of CO over a 4 h photothermal catalytic process, with a productivity rate approximating 216.9 $\mu mol \cdot g^{-1} \cdot h^{-1}$. Theoretically, this translates to a staggering 95% conversion efficiency of atmospheric CO_2, a remarkable achievement. Figure S4 demonstrates that the system's output is predominantly CO, with carbon monoxide constituting 97.8% of the generated products, indicating exceptionally high selectivity for CO.

$$\text{transformation rate} = \frac{\text{CO}}{\text{CO}_2 \text{ in the reactorir}} = \frac{491.6}{\text{CO}_2 \text{ in the air} + \text{CO}_2 \text{ adsorption quantity}} = \frac{491.6}{517.5} = 95\%$$

Under photothermal conditions, the reduction of CO_2 to CO is significantly accelerated, with reaction yields far surpassing the combined outputs achievable through sole photocatalysis or thermocatalysis. This underscores the synergistic effect at play, where the two catalytic mechanisms complement each other to produce optimal results. Moreover, a stability cycle test was conducted, revealing that even in the sixth cycle spanning four hours, the system managed to generate 714.3 $\mu mol \cdot g^{-1}$ of CO (Figure 6E). After a continuous 24 h reaction period, the stability of the system remained above 80%, further validating its robustness and reliability.

Moreover, compared to most previous studies on photothermal catalysis (refer to Table 1), our composite material exhibits superior performance. The analysis highlights the innovation and efficiency of BW-3MX in converting carbon dioxide to carbon monoxide at lower temperatures. This positions it as a promising candidate for sustainable and cost-effective carbon dioxide reduction strategies.

Table 1. Recent literature reports on photothermal catalysis CO_2 reduction.

Catalyst	Reaction Temperatures (°C)	Production Rate	Ref.
BiW-M	119.85	CO: 23.42 $\mu mol \cdot g^{-1} \cdot h^{-1}$	[46]
1T/2H-MoS_2	200	CO: 35.3 $\mu mol \cdot g^{-1} \cdot h^{-1}$	[47]
0.5BWO/3NiMU2	250	CO: 4493 $\mu mol \cdot g^{-1} \cdot h^{-1}$	[48]
TiO_2PNT	500	CO: 11.05 $\mu mol \cdot g^{-1} \cdot h^{-1}$	[49]
BW-3MX	80	CO:216.9 $\mu mol \cdot g^{-1} \cdot h^{-1}$	This work

2.8. Photothermal Catalytic Mechanism

The photothermal catalytic process involves a series of consecutive redox reactions on the catalyst, driven by the synergistic effects of light intensity and thermal energy (Figure 7). Under simulated solar irradiation, photogenerated electrons in Bi_2WO_6 are excited and transition from the valence band (VB) to the conduction band (CB). In this study, the valence and conduction bands of BW were determined using mass spectrometry

(MS), as illustrated in Figure S2. After reviewing the relevant literature, we confirmed the Fermi level of MXene [32]. Since the conduction band potential of Bi_2WO_6 is more negative than the Fermi level (E_F) of MXene, electrons can effectively migrate from Bi_2WO_6 to MXene, leading to an accumulation of electrons on the MXene surface. However, under illumination, MXene exhibits low excitation levels, making it less reactive and consequently limiting its catalytic activity. When thermal energy is introduced, the thermal effect of MXene accelerates electron transfer between Bi_2WO_6 and MXene, reducing the likelihood of electron-hole recombination and increasing the rate of redox reactions. Thermal energy activates MXene, significantly increasing the number of photogenerated electrons and holes. This synergistic interaction between light and heat enables more efficient and rapid migration of photogenerated electrons from the Bi_2WO_6 matrix to the MXene surface. As a result, this combined approach significantly enhances the overall photocatalytic CO_2 reduction efficiency, allowing for a more effective conversion of CO_2 into useful fuels or chemicals under realistic solar conditions.

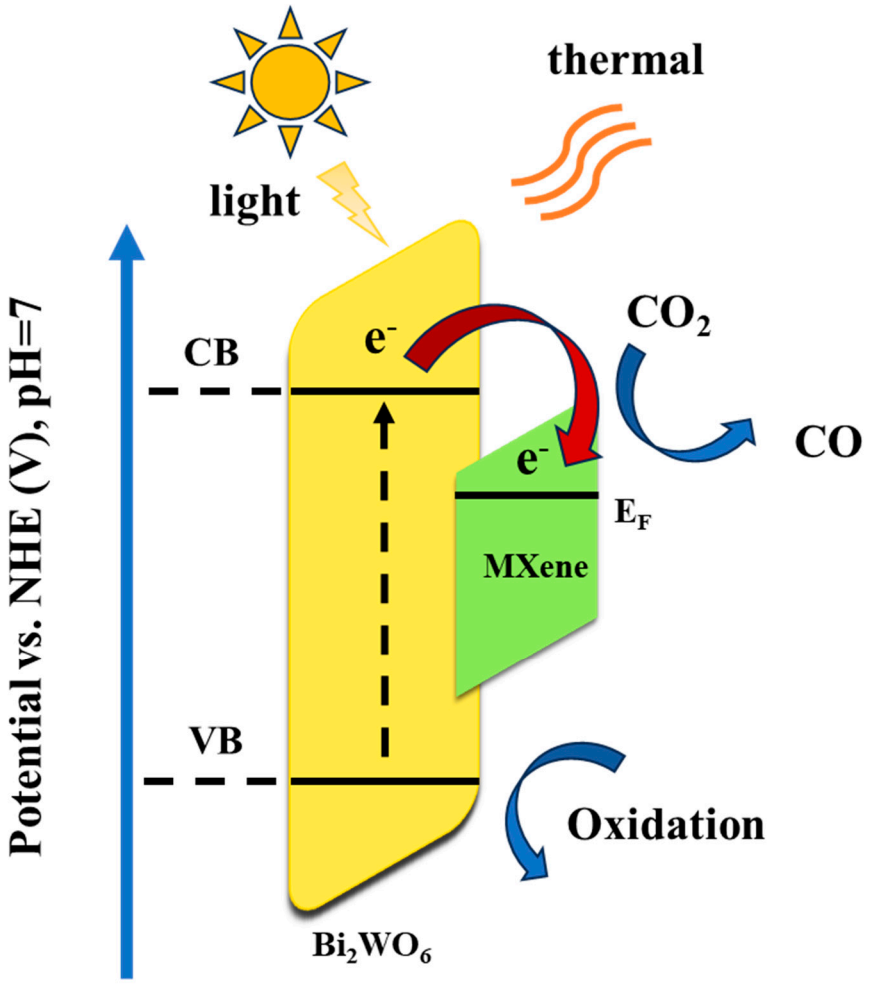

Figure 7. Energy level structure diagram of Bi_2WO_6 and MXene.

3. Experimental

3.1. Chemical Agents

The primary chemicals and reagents used in this study include sodium tungstate dihydrate ($Na_2WO_4 \cdot 2H_2O$, AR, 99.5%), bismuth nitrate pentahydrate ($Bi(NO_3)_3 \cdot 5H_2O$, AR, 99%), cetyltrimethylammonium bromide (CTAB, $C_{19}H_{42}BrN$, 99%), titanium aluminum carbide powder (Ti_3AlC_2, 99%), and hydrofluoric acid (HF, AR). The reagents used in the experimental procedure were purchased directly from Shanghai Aladdin Biochemical Technology Co., Ltd. (Shanghai, China).

3.2. Catalysts Preparation

3.2.1. Preparation of Layered Ti_3C_2 MXene

Initially, 5 g of Ti_3AlC_2 powder was gradually added to 60 mL of 40% hydrofluoric acid (HF) solution, taking care to control the rate of addition to prevent excessive reactions. To achieve complete etching of the Al layers, the mixture was continuously stirred at room temperature for 48 h. The resulting dark solution was then repeatedly washed with deionized water and anhydrous ethanol until a pH of 7 was reached. The final product was vacuum-dried at 60 °C for 6 h, yielding layered Ti_3C_2 MXene.

3.2.2. Preparation of Bi_2WO_6/MXene

Within a beaker filled with 30 mL of ultrapure water, 0.369 mol of $Na_2WO_4{\cdot}2H_2O$ and 30 mg of CTAB, along with a specific amount of MXene, were added. The mixture was stirred for 30 min, followed by ultrasonic treatment for an additional 30 min to obtain solution A. Subsequently, 0.738 mol of $Bi(NO_3)_3{\cdot}5H_2O$ was carefully added to 25 mL of ultrapure water, followed by continuous stirring to achieve a fully homogeneous mixture, designated as solution B. Solution A was combined with solution B, and the resulting mixture was mixed thoroughly for 3 h to ensure complete reaction and uniformity of the final solution. The prepared mixture was then transferred to a 100 mL Teflon-lined autoclave and subjected to reaction at 180 °C for 16 h. Upon completion, the product was thoroughly washed with ultrapure water and anhydrous ethanol to remove any residual reactants, followed by drying to yield a gray precipitate. The theoretical mass of Bi_2WO_6 was calculated, and the mass ratios of Bi_2WO_6 to MXene were adjusted to 100:1, 100:2, 100:3, 100:4, and 100:5, designated as BW-1MX, BW-2MX, BW-3MX, BW-4MX, and BW-5MX, respectively. For comparison, a gray-white substance was synthesized using the same procedure without the addition of MXene, designated as BW. Composite materials of all proportions are collectively referred to as BW-MX. All collected powders were stored in the dark to protect them from light exposure.

3.3. Characterization

The morphological characteristics and element distribution information were thoroughly investigated utilizing scanning electron microscopy (SEM; JSM-7001F) integrated with energy-dispersive X-ray spectroscopy (EDS). The internal microstructures, nanometer-scale characteristics, and element distribution were further examined by high-resolution transmission electron microscopy (HRTEM; FEI TF20), also equipped with EDS. The crystal structure was precisely analyzed through X-ray diffraction (XRD; Bruker D8ADVANCE (Billerica, MA, USA)) employing Cu Kα radiation. The optical absorption range and bandgap structure were determined by ultraviolet–visible diffuse reflectance spectroscopy (UV–Vis DRS; UH-4150). The Brunauer–Emmett–Teller (BET; Maxwell 2640) method was utilized to characterize nitrogen (N_2) and CO_2 adsorption–desorption curves, specific surface area, pore volume, and pore size distribution. The surface chemical composition and valence states were analyzed via X-ray photoelectron spectroscopy (XPS; ESCALAB 250Xi (Thermo Fisher Scientific, Waltham, MA, USA)). Photoluminescence (PL) spectra were recorded using a fluorescence spectrophotometer (FLS980, Livingston, UK). Electrochemical impedance spectroscopy (EIS), photocurrent, and Mott-Schottky (M-S) tests were conducted on an electrochemical workstation (Chi660e; Shanghai Chenhua (Shanghai, China)). Finally, the composition and content of photocatalytic products were analyzed by gas chromatography (GC, Shanghai Tianmei-GC-7980 (Shanghai, China)) and gas chromatography-mass spectrometry (GC–MS, Agilent 7980A-5975C (Tokyo, Japan)), ensuring a comprehensive understanding of the material's properties and performance.

3.4. Catalytic Reduction Process of Atmospheric CO_2

This study employs a photothermal catalytic system operating at the gas–solid interface, where a fixed bed coated with catalyst materials is positioned directly opposite the light source to facilitate photothermal catalytic reduction reactions. The system consists of

a reaction chamber with an intermediate layer capable of passing circulating water, a heat source for controlling the temperature of the circulating water, a tightly sealed top cover equipped with inlet and outlet ports, a fixed catalyst bed, a valve for sampling, a xenon lamp light source, and a quartz window.

The catalyst (5 mg, at room temperature) was evenly applied to the surface of the fixed catalyst bed. To facilitate an adequate equilibration of the reaction chamber with the ambient atmosphere, the chamber was left unsealed at a ventilated location for 30 min to allow for complete air filling. Subsequently, it was sealed to commence the experiments. The temperature in the reaction chamber was stabilized at 80 °C using water circulation. A 300 W xenon lamp, equipped with an AM 1.5 filter, simulated light conditions with an irradiance of approximately 200 $mW \cdot cm^{-2}$ for the photothermal catalytic reaction. Before the reaction, the gas in the closed reaction chamber was measured by GC–MS as a blank sample for the analysis of CO_2 content. The blank sample of evaluation is shown in Table 2. Similar procedures were followed for individual photocatalytic and thermal catalytic reactions. Gas chromatography (GC) was used to monitor catalytic products on an hourly basis, whereas gas chromatography–mass spectrometry (GC–MS) was utilized to analyze the ^{13}C-labeled photothermal catalytic products.

Table 2. Average blank sample.

Air composition	CO	CO_2	N_2	H_2	O_2
Content (ppm)	3	421	780,491	0.5	209,903

4. Conclusions

In summary, this study successfully synthesized Bi_2WO_6/MXene($Ti_3C_2T_x$) nanosheets using a hydrothermal method. The composite consists of multiple atomic layers of Bi_2WO_6 and MXene. Leveraging the synergistic effects of light and heat, this material facilitates the swift capture and transformation of atmospheric CO_2 at the gas–solid interface. Experimental results demonstrate that, under photothermal catalytic conditions for 4 h, the catalyst can produce 876.7 $\mu mol \cdot g^{-1}$ of CO. Theoretically, the CO_2-to-CO conversion efficiency in air can reach up to 95%. Moreover, it exhibits exceptionally high selectivity, with CO comprising 97.8% of the reaction products. This study underscores the potential of Bi_2WO_6 in photothermal synergistic catalysis, as well as the promise of MXene as a cost-effective and efficient co-catalyst. The high selectivity for CO_2 reduction at the gas–solid interface further demonstrates the feasibility of this approach for future practical applications, offering a strategic pathway for efficient CO_2 removal.

Supplementary Materials: The following supporting information can be downloaded at: https://www.mdpi.com/article/10.3390/catal14120859/s1. Figure S1: K-M curves of BW; Figure S2: M-S curves of BW; Figure S3: Thermal catalytic effect diagram at different temperatures; Figure S4: The detailed band structure of catalysts; Figure S5: Comparison of CO and CH4 production; Figure S6: Photothermal catalysis raw data.

Author Contributions: Conceptualization, H.Z.; data curation, L.Z. and Y.M. (Yang Meng); formal analysis, L.Z., M.S., Y.M. (Yang Meng) and C.L.; funding acquisition, M.B., Y.M. (Yongpeng Ma) and H.Z.; investigation, W.L.; methodology, L.Z., M.S. and H.Z.; resources, S.Z. (Shuo Zhang), M.B., S.Z. (Silvia Zamponi) and Y.M. (Yongpeng Ma); software, S.Z. (Shuo Zhang), S.Z. (Silvia Zamponi) and F.Y.; supervision, C.Y., Y.M. (Yongpeng Ma) and H.Z.; validation, L.Z., M.S.; writing—original draft, L.Z.; writing—review and editing, L.Z. All authors have read and agreed to the published version of the manuscript.

Funding: This study was supported by the Henan Collaborative Innovation Center of Environmental Pollution Control and Ecological Restoration (NO. 16403000001) and the Program for Science & Technology Innovation Team in Zhengzhou University of Light Industry (23XNKJTD0208).

Data Availability Statement: The original contributions presented in this study are included in the article/Supplementary Material. Further inquiries can be directed to the corresponding authors.

Conflicts of Interest: The authors declare no conflict of interest.

References

1. Qin, J.; Gong, N. The estimation of the carbon dioxide emission and driving factors in China based on machine learning methods. *Sustain. Prod. Consum.* **2022**, *33*, 218–229. [CrossRef]
2. Hao, J.; Chen, L.; Zhang, N. A Statistical Review of Considerations on the Implementation Path of China's "Double Carbon" Goal. *Sustainability* **2022**, *14*, 11274. [CrossRef]
3. Hong, C.; Burney, J.A.; Pongratz, J.; Nabel, J.; Mueller, N.D.; Jackson, R.B.; Davis, S.J. Global and regional drivers of land-use emissions in 1961–2017. *Nature* **2021**, *589*, 554–561. [CrossRef] [PubMed]
4. Zhu, T.; Liu, X.; Wang, X.; He, H. Technical Development and Prospect for Collaborative Reduction of Pollution and Carbon Emissions from Iron and Steel Industry in China. *Engineering* **2023**, *31*, 37–49. [CrossRef]
5. Dziejarski, B.; Serafin, J.; Andersson, K.; Krzyżyńska, R. CO_2 capture materials: A review of current trends and future challenges. *Mater. Today Sustain.* **2023**, *24*, 100483. [CrossRef]
6. Abdelhamid, H.N. Removal of carbon dioxide using zeolitic imidazolate frameworks: Adsorption and conversion via catalysis. *Appl. Organomet. Chem.* **2022**, *36*, e6753. [CrossRef]
7. Park, J.H.; Yang, J.; Kim, D.; Gim, H.; Choi, W.Y.; Lee, J.W. Review of recent technologies for transforming carbon dioxide to carbon materials. *Chem. Eng. J.* **2022**, *427*, 130980. [CrossRef]
8. Jia, X.; Zhang, Y.; Tan, R.R.; Li, Z.; Wang, S.; Wang, F.; Fang, K. Multi-objective energy planning for China's dual carbon goals. *Sustain. Prod. Consum.* **2022**, *34*, 552–564. [CrossRef]
9. Li, S.; Wang, S.; Wu, Q.; Zhang, Y.; Ouyang, D.; Zheng, H.; Han, L.; Qiu, X.; Wen, Y.; Liu, M.; et al. Emission trends of air pollutants and CO_2 in China from 2005 to 2021. *Earth Syst. Sci. Data* **2023**, *15*, 2279–2294. [CrossRef]
10. Garba, M.D.; Usman, M.; Khan, S.; Shehzad, F.; Galadima, A.; Ehsan, M.F.; Ghanem, A.S.; Humayun, M. CO_2 towards fuels: A review of catalytic conversion of carbon dioxide to hydrocarbons. *J. Environ. Chem. Eng.* **2021**, *9*, 104756. [CrossRef]
11. He, M.; Sun, Y.; Han, B. Green Carbon Science: Efficient Carbon Resource Processing, Utilization, and Recycling towards Carbon Neutrality. *Angew. Chem. Int. Ed. Engl.* **2022**, *61*, e202112835. [CrossRef] [PubMed]
12. Lu, Q.; Wu, H.; Zheng, X.; Chen, Y.; Rogach, A.L.; Han, X.; Deng, Y.; Hu, W. Encapsulating Cobalt Nanoparticles in Interconnected N-Doped Hollow Carbon Nanofibers with Enriched Co–N–C Moiety for Enhanced Oxygen Electrocatalysis in Zn-Air Batteries. *Adv. Sci.* **2021**, *8*, e2101438. [CrossRef] [PubMed]
13. Mateo, D.; Cerrillo, J.L.; Durini, S.; Gascon, J. Fundamentals and applications of photo-thermal catalysis. *Chem. Soc. Rev.* **2022**, *51*, 1547. [CrossRef] [PubMed]
14. Xu, C.; Huang, W.; Li, Z.; Deng, B.; Zhang, Y.; Ni, M.; Cen, K. Photothermal Coupling Factor Achieving CO_2 Reduction Based on Palladium-Nanoparticle-Loaded TiO2. *ACS Catal.* **2018**, *8*, 6582–6593. [CrossRef]
15. Zhang, J.; Li, Y.; Sun, J.; Chen, H.; Zhu, Y.; Zhao, X.; Zhang, L.-C.; Wang, S.; Zhang, H.; Duan, X.; et al. Regulation of energetic hot carriers on Pt/TiO_2 with thermal energy for photothermal catalysis. *Appl. Catal. B Environ.* **2022**, *309*, 121263. [CrossRef]
16. Ma, R.; Sun, J.; Li, D.H.; Wei, J.J. Review of synergistic photo-thermo-catalysis: Mechanisms, materials and applications. *Int. J. Hydrogen Energy* **2020**, *45*, 30288–30324. [CrossRef]
17. Li, P.; Liu, L.; An, W.; Wang, H.; Guo, H.; Liang, Y.; Cui, W. Ultrathin porous g-C3N4 nanosheets modified with AuCu alloy nanoparticles and C-C coupling photothermal catalytic reduction of CO to ethanol. *Appl. Catal. B Environ.* **2020**, *266*, 118618. [CrossRef]
18. Yang, Y.; Zhao, S.; Cui, L.; Bi, F.; Zhang, Y.; Liu, N.; Wang, Y.; Liu, F.; He, C.; Zhang, X. Recent advancement and future challenges of photothermal catalysis for VOCs elimination: From catalyst design to applications. *Green Energy Environ.* **2023**, *8*, 654–672. [CrossRef]
19. Xiao, Z.; Li, P.; Zhang, H.; Zhang, S.; Tan, X.; Ye, F.; Gu, J.; Zou, J.-J.; Wang, D. A comprehensive review on photo-thermal co-catalytic reduction of CO_2 to value-added chemicals. *Fuel* **2024**, *362*, 130906. [CrossRef]
20. Hepburn, C.; Adlen, E.; Beddington, J.; Carter, E.A.; Fuss, S.; Mac Dowell, N.; Minx, J.C.; Smith, P.; Williams, C.K. The technological and economic prospects for CO_2 utilization and removal. *Nature* **2019**, *575*, 87–97. [CrossRef]
21. Jiang, X.; Chen, S.; Zhang, X.; Qu, L.; Qi, H.; Wang, B.; Xu, B.; Huang, Z. Carbon-doped flower-like Bi_2WO_6 decorated carbon nanosphere nanocomposites with enhanced visible light photocatalytic degradation of tetracycline. *Adv. Compos. Hybrid Mater.* **2022**, *6*, 47. [CrossRef]
22. Zhu, Z.; Wan, S.; Zhao, Y.; Qin, Y.; Ge, X.; Zhong, Q.; Bu, Y. Recent progress in Bi_2WO_6-Based photocatalysts for clean energy and environmental remediation: Competitiveness, challenges, and future perspectives. *Nano Sel.* **2020**, *2*, 187–215. [CrossRef]
23. Cao, S.; Shen, B.; Tong, T.; Fu, J.; Yu, J. 2D/2D Heterojunction of Ultrathin MXene/Bi_2WO_6 Nanosheets for Improved Photocatalytic CO2 Reduction. *Adv. Funct. Mater.* **2018**, *28*, 1800136. [CrossRef]
24. Ju, P.; Wang, P.; Li, B.; Fan, H.; Ai, S.; Zhang, D.; Wang, Y. A novel calcined $Bi_2WO_6/BiVO_4$ heterojunction photocatalyst with highly enhanced photocatalytic activity. *Chem. Eng. J.* **2014**, *236*, 430–437. [CrossRef]
25. Liu, D.; Zeng, M.; Li, Z.; Zhu, Z.; Chen, Y.; Thummavichai, K.; Ola, O.; Wang, N.; Zhu, Y. Interfacial construction of $P25/Bi_2WO_6$ composites for selective CO_2 photoreduction to CO in gas-solid reactions. *RSC Adv.* **2023**, *13*, 8564–8576. [CrossRef]
26. Ikreedeegh, R.R.; Tahir, M. A critical review in recent developments of metal-organic-frameworks (MOFs) with band engineering alteration for photocatalytic CO_2 reduction to solar fuels. *J. CO2 Util.* **2021**, *43*, 101381. [CrossRef]

27. Hou, W.; Cronin, S.B. A Review of Surface Plasmon Resonance-Enhanced Photocatalysis. *Adv. Funct. Mater.* **2012**, *23*, 1612–1619. [CrossRef]
28. Naguib, M.; Kurtoglu, M.; Presser, V.; Lu, J.; Niu, J.; Heon, M.; Hultman, L.; Gogotsi, Y.; Barsoum, M.W. Two-dimensional nanocrystals produced by exfoliation of Ti3 AlC2. *Adv. Mater.* **2011**, *23*, 4248–4253. [CrossRef]
29. Sharif, H.M.A.; Rashad, M.; Hussain, I.; Abbas, A.; Aldosari, O.F.; Li, C. Green energy harvesting from CO_2 and NOx by MXene materials: Detailed historical and future prospective. *Appl. Catal. B Environ.* **2024**, *344*, 123585. [CrossRef]
30. Li, R.; Zhang, L.; Shi, L.; Wang, P. MXene Ti_3C_2: An Effective 2D Light-to-Heat Conversion Material. *ACS Nano* **2017**, mboxemph11, 3752–3759. [CrossRef]
31. Koneru, B.; Swapnalin, J.; Pothu, R.; Banerjee, P.; Boddula, R.; Radwan, A.B.; Al-Qahtani, N. Role of the intercalated ions on the high capacitance behavior of Ti3C2Tx MXene nanohybrids. *Nanocomposites* **2023**, *9*, 128–137. [CrossRef]
32. Kabir, L.; Wijaya, K.; Oh, W.-C. Progressive MXene-based photocatalytic and electrocatalytic sustainable reduction of CO2 to chemicals: Comprehensive review and future directions. *Sustain. Energy Fuels* **2024**, *8*, 2535–2569. [CrossRef]
33. Zong, S.; Liu, J.; Huang, Z.; Liu, L.; Liu, J.; Zheng, J.; Fang, Y. Mxene-TiO_2 composite with exposed {101} facets for the improved photocatalytic hydrogen evolution activity. *J. Alloys Compd.* **2022**, *896*, 163039. [CrossRef]
34. Li, Z.; Wu, Y. 2D Early Transition Metal Carbides (MXenes) for Catalysis. *Small* **2019**, *15*, e1804736. [CrossRef]
35. Zhao, D.; Cai, C. Layered Ti_3C_2 MXene modified two-dimensional Bi_2WO_6 composites with enhanced visible light photocatalytic performance. *Mater. Chem. Front.* **2019**, *3*, 2521–2528. [CrossRef]
36. Tan, D.; Cheng, X.; Zhang, J.; Sha, Y.; Shen, X.; Su, Z.; Han, B.; Zheng, L. Photocatalytic carbon dioxide reduction coupled with benzylamine oxidation over Zn-Bi_2WO_6 microflowers. *Green Chem.* **2021**, *23*, 2913–2917. [CrossRef]
37. Collado, L.; Gomez-Mendoza, M.; García-Tecedor, M.; Oropeza, F.E.; Reynal, A.; Durrant, J.R.; Serrano, D.P.; de la Peña O'Shea, V.A. Towards the improvement of methane production in CO2 photoreduction using Bi_2WO_6/TiO_2 heterostructures. *Appl. Catal. B Environ.* **2023**, *324*, 122206. [CrossRef]
38. Anjali, K.; Ganesh, V.; Christopher, J.; Sakthivel, A. Copper based macromolecular catalysts for the hydroxylation of phenols. *J. Organomet. Chem.* **2020**, *929*, 121579. [CrossRef]
39. Halim, J.; Cook, K.M.; Naguib, M.; Eklund, P.; Gogotsi, Y.; Rosen, J.; Barsoum, M.W. X-ray photoelectron spectroscopy of select multi-layered transition metal carbides (MXenes). *Appl. Surf. Sci.* **2016**, *362*, 406–417. [CrossRef]
40. Ran, J.; Gao, G.; Li, F.T.; Ma, T.Y.; Du, A.; Qiao, S.Z. Ti_3C_2 MXene co-catalyst on metal sulfide photo-absorbers for enhanced visible-light photocatalytic hydrogen production. *Nat. Commun.* **2017**, *8*, 13907. [CrossRef]
41. Shah, S.A.; Habib, T.; Gao, H.; Gao, P.; Sun, W.; Green, M.J.; Radovic, M. Template-free 3D titanium carbide (Ti3C2Tx) MXene particles crumpled by capillary forces. *Chem. Commun.* **2017**, *53*, 400–403. [CrossRef] [PubMed]
42. Zhang, Y.; Xu, C.; Chen, J.; Zhang, X.; Wang, Z.; Zhou, J.; Cen, K. A novel photo-thermochemical cycle for the dissociation of CO_2 using solar energy. *Appl. Energy* **2015**, *156*, 223–229. [CrossRef]
43. Jo, W.-K.; Kumar, S.; Eslava, S.; Tonda, S. Construction of Bi_2WO_6/RGO/g-C_3N_4 2D/2D/2D hybrid Z-scheme heterojunctions with large interfacial contact area for efficient charge separation and high-performance photoreduction of CO_2 and H_2O into solar fuels. *Appl. Catal. B Environ.* **2018**, *239*, 586–598. [CrossRef]
44. Yang, W.; Zhou, F.; Sun, N.; Wu, J.; Qi, Y.; Zhang, Y.; Song, J.; Sun, Y.; Liu, Q.; Wang, X.; et al. Constructing a 3D $Bi_2WO_6/ZnIn_2S_4$ direct Z-scheme heterostructure for improved photocatalytic CO_2 reduction performance. *J. Colloid. Interface Sci.* **2024**, *662*, 695–706. [CrossRef]
45. Thommes, M.; Kaneko, K.; Neimark, A.V.; Olivier, J.P.; Rodriguez-Reinoso, F.; Rouquerol, J.; Sing, K.S.W. Physisorption of gases, with special reference to the evaluation of surface area and pore size distribution (IUPAC Technical Report). *Pure Appl. Chem.* **2015**, *87*, 1051–1069. [CrossRef]
46. Yan, J.; Wang, C.; Ma, H.; Li, Y.; Liu, Y.; Suzuki, N.; Terashima, C.; Fujishima, A.; Zhang, X. Photothermal synergic enhancement of direct Z-scheme behavior of $Bi_4TaO_8Cl/W_{18}O_{49}$ heterostructure for CO_2 reduction. *Appl. Catal. B Environ.* **2020**, *268*, 118401. [CrossRef]
47. Wang, Y.; Lin, Y.; Zha, F.; Li, Y. Heterophase junction engineering: Enhanced photo-thermal synergistic catalytic performance of CO_2 reduction over 1T/2H-MoS_2. *J. Colloid. Interface Sci.* **2023**, *652*, 936–944. [CrossRef]
48. Wu, J.; Li, K.; An, S.; Yan, S.; Liu, J.; Song, C.; Guo, X. An S-scheme heterojunction of single Ni sites decorated ultrathin carbon nitride and Bi_2WO_6 for highly efficient photothermal CO_2 conversion to syngas. *Appl. Catal. B Environ. Energy* **2024**, *347*, 123822. [CrossRef]
49. Li, D.; Huang, Y.; Li, S.; Wang, C.; Li, Y.; Zhang, X.; Liu, Y. Thermal coupled photoconductivity as a tool to understand the photothermal catalytic reduction of CO_2. *Chin. J. Catal.* **2020**, *41*, 154–160. [CrossRef]